

Off-Center Collisions between Clusters of Galaxies

P. M. Ricker

Department of Astronomy, University of Virginia, Charlottesville, VA 22903

ABSTRACT

We present numerical simulations of off-center collisions between galaxy clusters made using a new hydrodynamical code based on the piecewise-parabolic method (PPM) and an isolated multigrid potential solver. The current simulations follow only the intracluster gas. We have performed three high-resolution (256×128^2) simulations of collisions between equal-mass clusters using a nonuniform grid with different values of the impact parameter (0, 5, and 10 times the cluster core radius). Using these simulations we have studied the variation in equilibration time, luminosity enhancement during the collision, and structure of the merger remnant with varying impact parameter.

We find that in off-center collisions the cluster cores (the inner regions where the pressure exceeds the ram pressure) behave quite differently from the clusters' outer regions. A strong, roughly ellipsoidal shock front, similar to that noted in previous simulations of head-on collisions, enables the cores to become bound to each other by dissipating their kinetic energy as heat in the surrounding gas. These cores survive well into the collision, dissipating their orbital angular momentum via spiral bow shocks. After the ellipsoidal shock has passed well outside the interaction region, the material left in its wake falls back onto the merger remnant formed through the inspiral of the cluster cores, creating a roughly spherical accretion shock. For less than one-half of a sound crossing time after the cores first interact the total X-ray luminosity increases by a large factor; the magnitude of this increase depends sensitively on the size of the impact parameter.

Observational evidence of the ongoing collision, in the form of bimodality and distortion in projected X-ray surface brightness and temperature maps, is present for 1–2 sound crossing times after the collision, but only for special viewing angles. The remnant actually requires at least five crossing times to reach virial equilibrium. Since the sound crossing time can be as large as 1–2 Gyr, the equilibration time can thus be a substantial fraction of the age of the universe. The final merger remnant is very similar for impact parameters of zero and five core radii. It possesses a roughly isothermal core, with central density and temperature twice the initial values for the colliding clusters. Outside the core the temperature drops as r^{-1} , and the density roughly as $r^{-3.8}$. The core radius shows a small increase due to shock heating during the merger. For an impact parameter of ten core radii the core of the remnant possesses a more flattened density profile, with a steeper dropoff outside the core. In both off-center cases the merger remnant rotates, but only for the ten-core-radius case does this appear to have an effect on the structure of the remnant.

Subject headings: Galaxies: clusters: general — hydrodynamics — intergalactic medium
— methods: numerical — X-rays: galaxies

1. Introduction

Galaxy clusters are the largest bound structures in the present-day universe. However, they are not the oldest. For galaxy clusters the notion of ‘age’ does not necessarily refer to the time elapsed since a specific formation event occurred, after which they remained either static in their properties or very slowly evolving. Indeed, a growing body of observational and theoretical evidence indicates that for many clusters ‘formation’ means an ongoing sequence of mergers and interactions with other clusters. Understanding this process is important not only from the standpoint of understanding cluster evolution, but also because of its implications for cosmology.

Recent ROSAT and ASCA observations of rich clusters of galaxies have shown that many of them are either in the process of merging with another cluster or have recently undergone such a merger. The ROSAT results, because of poor spectral resolution but good spatial resolution, emphasize the variation in gas density and hence the depth of the potential well in a cluster. These include observations of the Coma cluster (White, Briel, & Henry 1993), Abell 2256 (Briel et al. 1991), and Abell 2163 (Elbaz, Arnaud, & Böhringer 1995). The signatures of merging events in these observations include distorted X-ray isophotes (presumably elongated along the collision axes); offsets of the gas centroid, as indicated by the X-ray emission, and the center of mass of the galaxy distribution; and bimodal distributions of emission. The ROSAT results are consistent with earlier results from Einstein observations which suggested that at least 22% of clusters show significant X-ray substructure (Forman & Jones 1994). In the more recent ASCA observations of Abell 754 (Henriksen & Markevitch 1996), which emphasize the variation in gas temperature through its influence on the X-ray spectrum, the presence of a ridge of high-temperature emission has been taken as indicative of an ongoing merger event. However, significant temperature variations have not been seen by ASCA in other merger candidates identified from ROSAT data, including Abell 2256 and Abell 2163 (Markevitch 1996).

Although we do not yet completely understand the physical mechanisms behind and cosmological implications of galaxy cluster mergers, it is not surprising that they should occur frequently. In hierarchical models of large-scale structure formation, objects like galaxy clusters form through the merging and then ac-

cretion of smaller clumps of matter. In these models the present-day fraction of clusters which have significant substructure can give us constraints on the value of the density parameter Ω (Richstone, Loeb, & Turner 1992), and the mass density profiles resulting from mergers provide information about the spectrum of primordial density fluctuations (Hoffman & Shalam 1985). However, although analytical approaches based on the spherical top-hat model and the Press-Schechter (1974) mass function have provided much insight into these implications, the complex physical interactions present during a cluster merger can only be studied adequately through numerical simulation.

To date simulations of galaxy cluster evolution (either N -body or mesh-based) have typically followed one of three approaches. Some simulations have focused on the collapse and relaxation of a single overdense region which has been prepared as a ‘typical’ example given a large-scale structure model (e. g. Evrard 1990; Evrard, Metzler, & Navarro 1996). Others have produced clusters within large-scale structure simulations, then followed their evolution separately from the rest with greater spatial resolution (e. g. Katz & White 1993). Both types of simulation produce realistic clusters in an environment which permits comparison of large-scale structure theories but which renders analysis of individual merging events difficult because of the uncontrolled initial conditions for each event and the frequent occurrence of multiple simultaneous mergers.

A third type of cluster evolution simulation has focused on collisions of idealized clusters or subclusters (e. g. Roettiger, Burns, & Loken 1993; Schindler & Müller 1993; Pearce, Thomas, & Couchman 1994; Roettiger, Stone, & Mushotzky 1997) to gain insight into the merger process without complicating the problem with multiple mergers. This approach also permits mergers to be studied with better resolution than is possible in large-scale structure simulations.

Roettiger et al. (1993) simulated the head-on collision of two King-model clusters of unequal mass using the ZEUS-3D finite-difference code with a nonuniform grid for the gas dynamics and the Hernquist (1987) treecode for the dark matter. The resolution of these simulations was such that the smallest zones were one-half the core radius of the smaller cluster. During the collision they observed a double-peaked X-ray emission profile and a bar of X-ray emission perpendicular to the collision axis which resulted from a strong cen-

tral shock (Mach number ~ 4). They also observed a high-velocity (~ 2800 km/s), ordered flow of gas through the center of the dominant cluster which they suggested might disrupt cooling flows and be responsible for the bending of radio jets in cluster galaxies. Although their simulation did not include cooling, a later simulation by Burns et al. (1994) of a collision between the Coma cluster and the NGC 4839 group, using the same code but including cooling and having somewhat higher core resolution, obtained similar results.

Schindler and Müller (1993) also studied head-on collisions derived from slightly less controlled initial conditions using the piecewise-parabolic method (PPM) for the gas dynamics and Aarseth's (1972) code for collisionless galaxy halos. During the course of their collisions they observed multiple interacting shocks which led to X-ray luminosity enhancements of about a factor of 1.5 and temperature enhancements of a factor of 5, with a non-isothermal final state as the result. These calculations used a uniform grid with about 2.5 cells per core radius.

Neither Roettiger et al. (1993), Burns et al., nor Schindler and Müller included the baryonic contribution to the gravitational potential, thus limiting their conclusions to gas-poor clusters (less than 5%–10% of the total mass). However, some clusters can have as much as 30% (for a Hubble constant of $50 \text{ km s}^{-1} \text{ Mpc}^{-1}$) of their total mass in the intracluster medium (David, Jones, & Forman 1995; White & Fabian 1995). The virial estimates of total cluster masses on which this ROSAT finding is based are supported by recent simulation work by Evrard et al. (1996). The gas in these clusters may therefore have a significant effect on the potential, rendering a self-consistent treatment necessary.

Pearce et al. (1994) performed head-on collision simulations of equal-mass clusters using an adaptive smoothed-particle hydrodynamics (SPH) code which does include both gas and dark matter in the potential. They found that the gas, which made up $1/8$ of their clusters' total mass, tends to produce an extended constant-density core after the collision, whereas the dark matter component does not. However, while they note the presence of shocks due to the collision of the gas components of the clusters, they do not discuss the observational appearance of the merging system in detail or compare it to the finite-difference results. More recently, Roettiger et al. (1997) have used a PPM/particle-mesh code to

simulate a collision intended to reproduce the observations of A754, varying collision parameters at low resolution and then resimulating with the most promising parameter values at high resolution.

With the exception of Roettiger et al. (1997), none of these authors have considered off-center collisions in detail, although Pearce et al. mention that preliminary results from such simulations indicate that the gas receives additional support from rotation in the merger remnant. Interest in off-center collisions is growing, however, as ASCA temperature maps of clusters such as A754 (Henriksen & Markevitch 1996) begin to give us more detailed information about off-center cluster mergers in progress. The net angular momentum imparted to a cluster by many such collisions is probably small, since the angular momenta brought by collisions in different directions will tend to cancel each other out. Also, the net spins induced in collapsed objects by tidal torques due to inhomogeneities in the large-scale mass distribution have been shown to be small (Peebles 1993). However, during their pre-collision evolution, colliding subclusters should experience some deflection due to distant collisions with other subclusters. Given the great difference in behavior to be expected between the limiting cases of a simple distant deflection and a head-on collision, we would do well to consider the dynamics of intermediate cases and its effects on the long-term evolution and observable properties of clusters.

In order to study galaxy cluster evolution, and in particular off-center collisions of galaxy clusters, we have developed a parallel hydrodynamics code based on PPM which self-consistently solves for the gravitational potential of the gas using a multigrid algorithm with isolated boundary conditions. The code uses a nonuniform grid, permitting it to resolve the inner regions of the colliding clusters while simultaneously tracking the development of the shocks which result from the collision. We have added radiative cooling and linked the PPM code to a particle-mesh N -body solver for dark matter (written by Scott Dodelson), but the simulations described in this paper include only nonradiating gas. While these gas-only calculations necessarily exclude the substantial contribution of collisionless effects to cluster evolution, they nevertheless represent an important benchmark for more realistic calculations including dark matter, because it is far more straightforward to understand both the physical and numerical properties of the hydrodynamical results in isolation. This is analogous

to the approach taken prior to the advent of combined N -body/hydro codes, in which the collisionless dynamics of the dark matter was studied in isolation using N -body codes with well-understood properties. In a forthcoming paper we will discuss simulations performed with our new hybrid code, using the results presented here as a basis of comparison.

The paper is organized as follows. Section 2 gives a brief description of the code and the initial and boundary conditions used; a more complete description, including the equations used and the results of running the code on several standard test problems, will be presented in another forthcoming paper. Section 3 describes a resolution study performed using a single cluster at rest at the center of the grid. Section 4 describes results from three high-resolution simulations of collisions between equal-mass clusters at different impact parameters. Section 5 discusses the equilibration times and X-ray brightening observed in these calculations, as well as the thermal and rotational properties of the merger remnants. Section 6 summarizes our conclusions.

2. Numerical methods

2.1. Hydrodynamics

To solve the equations of hydrodynamics for the cluster gas we use the direct Eulerian formulation of the piecewise-parabolic method (PPM; Colella & Woodward 1984) on a nonuniform Cartesian grid. In contrast to most numerical studies of cluster evolution which use smoothed particle hydrodynamics (SPH) (e. g. Evrard 1990) for its ability to dynamically adjust spatial resolution, simulations using PPM offer better shock handling for comparable spatial resolution, since they require very little artificial viscosity. SPH resolves shocks only poorly and requires substantial amounts of artificial viscosity. Furthermore, in low-density regions where SPH represents the gas with relatively few particles, PPM obtains more accurate temperatures (Kang et al. 1994). The error properties of finite-volume methods in general, of which PPM is a specific example, are better understood than those of SPH. For these reasons we believe PPM to be the more appropriate method at present for studying the evolution of the collisional component of galaxy clusters.

Others have used PPM to study cluster evolution. Schindler and Müller (1993) used PPM together with the N -body solver of Aarseth (1972) to evolve the gas

in their simulation on a 60^3 uniform mesh covering little more than the two colliding clusters they studied. Bryan et al. (1994) used PPM on a much larger mesh with 270^3 cells to study the evolution of many poorly resolved clusters over a volume large enough to contain a statistical sample of clusters. Roettiger et al. (1993) used a non-Godunov-based finite-difference method similar to PPM in its use of parabolic interpolants to follow two merging clusters; their grid contained 187×65^2 cells and had nonuniform spacing which permitted good resolution of the cluster cores. More recently, Roettiger et al. (1997) have used a PPM/particle-mesh hybrid code to simulate the evolution of Abell 754 on a 512×256^2 grid with a maximum resolution of $1/10$ the cluster core radius.

However, with the exception of Bryan et al. and Roettiger et al. (1997), none of these authors self-consistently solved for the contribution of the gas to the potential. This is a serious shortcoming, one not shared by the SPH codes; even a gas mass fraction of 10% can significantly affect the potential on small scales if the gas and dark matter distributions are not the same. In our code we therefore include the gas density in the computation of the potential, which is described in the next subsection. Although the results presented here do not include dark matter, we have linked our hydrodynamical code to an N -body code based on the particle-mesh method, with the two codes sharing the same potential solver. We plan to report on results obtained with the new hybrid code in the near future. The new code also includes radiative cooling, which we do not include in the results presented here.

In order to look for observational signatures of recent on- or off-center merger events, one must be able to study a computational volume which is large enough to contain the shocks produced by the merger until they cease to be important. Furthermore, our single-cluster test runs, described in the next section, suggest that to do the problem correctly one must use a grid spacing in the inner regions of the clusters of at most one-half the core radius r_c . In order to begin to reconcile these two requirements we have used for our high-resolution runs a nonuniform grid of 256×128^2 zones. The innermost $N_{x,\text{inner}} = 192$ zones of the x -axis have uniform widths equal to $0.28r_c$. The innermost $N_{yz,\text{inner}} = 72$ zones in y and z have uniform widths equal to $0.39r_c$. Outside the uniformly gridded region in each coordinate direction the zone widths increase at the rate of 5% per zone as one moves away

from the center of the grid. The size of the uniformly gridded region was chosen to maximize resolution and minimize any effects due to grid nonuniformity in the region where most of the complex shocks form during the simulation. In terms of the initial cluster radius $R = 9r_c$, our computational grid has physical dimensions $11R \times 8.1R \times 8.1R$.

In test calculations of the Sedov-Taylor explosion problem (Sedov 1959) we have found that using first-order operator splitting to create a three-dimensional PPM scheme does not adequately maintain the 90-degree rotational symmetry of a uniform grid, particularly in the central part of the grid where a rarefied region develops in the Sedov-Taylor problem. We therefore use a second-order splitting, generalized from Strang (1968) to three dimensions. Although this doubles the cost of a hydrodynamical timestep relative to first-order splitting, the spherically symmetric, centrally concentrated nature of our initial density and pressure field makes it important to preserve this symmetry.

In a realistic simulation of cluster evolution, tides from mass concentrations outside of the grid would affect the simulated objects. Mass inflow through the grid boundaries would also be expected. However, in our simulations we are studying the behavior of a single merging system, so vacuum boundaries are appropriate. To implement these we use the standard zero-gradient boundaries with a slight difference. If purely zero-gradient boundaries are used, any inward-directed velocity in the interior zones adjacent to the boundary will result in a completely artificial inward mass flux. Since this mass flux adds to the depth of the potential, adding to the inward acceleration in these zones, this problem can destabilize the entire calculation. To prevent such artificial inward flows we modify the zero-gradient prescription when velocities in the interior zones adjacent to the boundaries are directed inward. For these zones we apply Dirichlet boundary conditions to the component of velocity normal to the boundary. All other variables, including velocity components parallel to the boundary, are given zero-gradient boundary conditions as usual. This suffices for the interpolation step in PPM; for the flux computation step we set the boundary flux of all conserved quantities (mass, momentum, and energy) to zero if it would otherwise be directed inward.

2.2. Gravitation

At each timestep of the hydrodynamical code we solve the Poisson equation for the gravitational potential using a full multigrid/nested iteration code (Brandt 1977; Hackbusch 1985). This method accelerates the convergence of standard elliptic relaxation techniques by iteratively solving on grids of increasing coarseness. Because long-wavelength errors are responsible for the slow convergence of standard iteration techniques, solving on coarse grids accelerates convergence by turning long-wavelength modes into short-wavelength modes. The resulting speedup is sufficient to make multigrid methods competitive with direct methods, such as those based on the fast Fourier transform, even for nonlinear equations or unusual boundary conditions.

In our case the primary reasons for using a multigrid method are the need for ease and portability of parallelization and the nature of the boundary conditions for our problem. FFT-based Poisson solvers are most efficient when working with periodic, Dirichlet, or Neumann boundaries on a uniform grid. However, in the colliding cluster problem, it is more natural to permit the potential to go to zero at infinity. Methods exist to handle these ‘isolated’ boundaries using direct solvers (e. g. James 1977) but suffer from the disadvantages of the direct methods on which they are based. To handle isolated boundaries with multigrid we have developed a method similar to that of James. We first obtain a solution with Dirichlet boundaries, then use this to compute image charges on the boundaries under the assumption that the potential is zero not only on the boundary but everywhere outside it as well. We then compute the isolated potential of the image charges and subtract it from the Dirichlet solution. To calculate the isolated potential of the image charges, we use a truncated spherical harmonic expansion of the image charge distribution about its center of mass to estimate boundary values for the potential, then solve Laplace’s equation in the interior using these boundary values. Although this method requires two calls to the multigrid solver, we only need to compute image moments and boundary values for points on the boundary. We have tested this potential solver with mass distributions drawn from collision runs performed on a nonuniform 128×64^2 grid similar to that described in the previous section, and we find that an acceptable compromise between computation time and accuracy is reached if one truncates the multipole expansion at $\ell = 10$. The typical change

in the potential ϕ in going to larger ℓ is less than 1%.

2.3. Initial conditions

We are interested in gaining insight into the physics of cluster collisions without the complication of initial conditions drawn from a large-scale structure simulation. By examining the parametric dependence of the observed features of such events we can later check cosmological theories by determining what distribution of collision parameters they produce. Accordingly we have chosen for our initial conditions nonsingular isothermal spheres, approximated by the modified Hubble law,

$$\rho(r) = \frac{\rho_0}{\left[1 + (r/r_c)^2\right]^{3/2}}, \quad (1)$$

where ρ_0 is the central mass density and r_c is the cluster core radius, as in the paper by Pearce et al. (1994). However, instead of truncating the distribution (1) beyond the radius $R = 16r_c$ as they did, we have used the smaller value of $9r_c$. The exact value of R/r_c , if it is of order 10 or so, is not important for the dynamics of the inner regions of the clusters, but it does affect our ability to resolve the cluster cores properly. We assume that the density perturbations which created the clusters have entered the strongly nonlinear regime well before the start of the simulation, so we use a background spacetime which is flat and nonexpanding. Since PPM is a finite-volume scheme which uses cell-averaged quantities (in contrast to a finite-difference scheme, which manipulates the values of fields at grid points), we set the density in each cell using Monte Carlo averaging of the density profile (1). The temperature is specified by the core radius and central number density via the standard definition of the core radius (Binney & Tremaine 1987):

$$\frac{kT_{\text{init}}}{\mu} = \frac{4}{9}\pi G\rho_0 r_c^2. \quad (2)$$

We set the pressure in each cell by Monte Carlo-averaging $\rho(r)T$ together with the density. To convert temperature to pressure we use

$$p = \frac{\rho kT_{\text{init}}}{\mu}, \quad (3)$$

where k is Boltzmann's constant. Here μ is different from the average atomic mass $\langle m \rangle$ because of the contribution of electrons to the gas pressure; assuming a

primordial composition (25% helium, 75% hydrogen by mass), we have $\mu \approx 0.59m_{\text{H}}$ and $\langle m \rangle \approx 1.2m_{\text{H}}$. As our gas is hot enough to be completely ionized, we use $\gamma = 5/3$ as our ratio of specific heats.

In the simulations presented here, both clusters have the same central density and core radius, hence the same mass and temperature. We use units in which each cluster initially has unit mass, unit radius, and unit temperature. The time unit is one sound crossing time,

$$t_{\text{sc}} \equiv \frac{R}{c_s} = 9r_c \sqrt{\frac{\mu}{\gamma kT_{\text{init}}}}, \quad (4)$$

so in our units the initial sound speed c_s is also unity. In these units the central density ρ_0 is approximately 30.5, and the core radius r_c is 1/9. The scaling of our simulations to physical units is determined by our choices for the values of m_{H}/k and Newton's gravitational constant G ; we use $m_{\text{H}}/k \approx 2.86t_{\text{sc}}^2 T_{\text{init}} R^{-2}$ and $G \approx 1.14R^3 M^{-1} t_{\text{sc}}^{-2}$. Outside the two clusters, the density is set to $10^{-8}\rho(R)$, and the temperature is the same as it is inside the clusters.

The two clusters are initialized with centers in the xy -plane, separated by a distance b_{init} (the impact parameter) in the y -direction and a distance d_{init} in the x -direction (Figure 1). For the calculations described here we performed three $256 \times 128 \times 128$ runs using different values of the impact parameter b_{init} . In run A, $b_{\text{init}} = 0$; in run B, $b_{\text{init}} = 5r_c$; and in run C, $b_{\text{init}} = 10r_c$. The value of d_{init} was held fixed at $4R$ for all of the runs, so that the clusters started close enough together to collide within a short time but far enough apart so that any numerical artifacts due to the initial conditions would be smoothed out before the cores interacted. The initial relative velocity, v_{init} ,

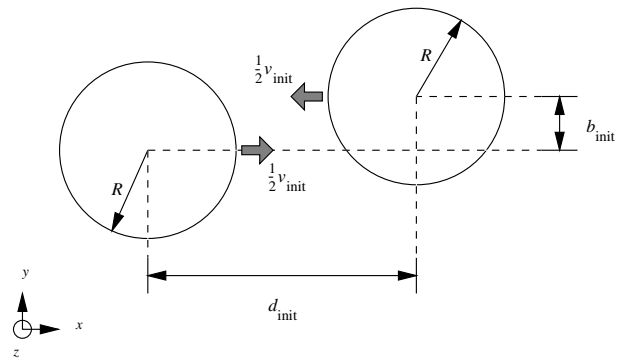


Fig. 1.— Initial conditions for cluster collision runs.

was chosen to be approximately equal to the free-fall velocity for the two clusters at a distance d_{init} , and was directed along the x -axis. All three runs used the same value for v_{init} (unity). The results of these runs are discussed in Sections 4 and 5.

3. Single-cluster tests

To study the behavior of our code on a simple yet realistic test problem, we simulated a single cluster at the center of a nonuniform grid similar to that used in our collision simulations. Since the gas density profile is approximately that of an isothermal sphere, these initial conditions should produce an approximately static configuration. We performed three runs at grid sizes of 32^3 (run T1), 64^3 (run T2), and 128^3 (run T3) using nonuniform gridding in all three dimensions. The physical box size was kept constant at $L \approx 6R$, and the grid nonuniformity, described in the previous section, was kept constant at 5%. This leaves the number of zones in the uniform inner region, N_{inner} , and the zone size in this region, Δ , as free parameters. The values of these parameters used in the test runs are summarized in Table 1. In each run the central density ρ_0 and core radius r_c were given the same values used in the collision runs. Varying the resolution in this way permitted us to determine how core resolution affects the accuracy of the solution in the central regions of the cluster, and also to control for the deviation of our initial conditions from true isothermal spheres in the collision runs.

Figure 2 presents the average kinetic (T), internal (U), and potential (W) energies of the cluster in each of the three test runs. For each run the total energy ($\mathcal{E} = T + U + W$), less the amount lost from the grid between $t = t_{\text{sc}}$ and $t = 3t_{\text{sc}}$, is constant to better than 1%, with the energy differing slightly between the runs because of slight differences in the size of the box used. However, in each run during the first 2–3 sound crossing times the internal and potential energies decrease in magnitude, and the kinetic energy briefly increases from zero. This occurs because our initial conditions contain an artificial shock where the Hubble-law profile is truncated. To keep the near vacuum outside the clusters in pressure equilibrium with the cluster, we would have to set the temperature in these regions to a very large value, forcing the timestep to be unacceptably small (via the Courant condition). We therefore allow a pressure gradient to exist at the edges of the cluster. Initially this gradi-

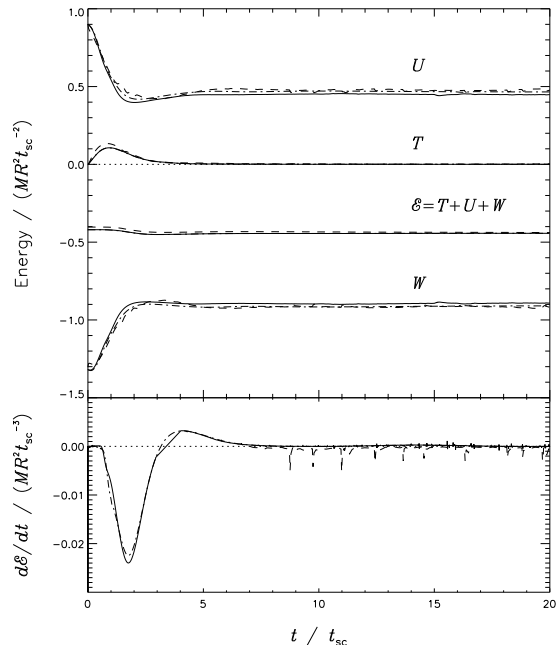


Fig. 2.— The upper plot shows the kinetic, internal, and potential energies in the single cluster tests. The total energy is also plotted. The lower plot shows the time derivative of the total energy. Dashed lines indicate run T1 (32^3), dot-dashed lines, run T2 (64^3), and solid lines, run T3 (128^3).

Table 1: Grid parameters used in the single-cluster test runs.

Run	Grid size	N_{inner}	Δ/r_c
T1	32^3	16	1.36
T2	64^3	32	0.582
T3	128^3	64	0.212

ent drives a rapid expansion of the ‘vacuum material’ outside the cluster. The cluster itself also expands, cooling by about a factor of two and driving about 15% of the total mass off the grid between $t = t_{\text{sc}}$ and $t = 3t_{\text{sc}}$. As the pressure gradient is relieved by this expansion, the expansion slows and stops. The material remaining on the grid briefly falls back toward the center of the cluster before reaching hydrostatic equilibrium. Because the computational box is not much larger than the cluster itself, at late times the density distribution in the ‘vacuum’ regions is not quite spherical. We use a larger box in the collision simulations to avoid this effect.

The time required for the cluster to reach virial equilibrium, as determined using the method described in Section 5, was approximately $(2-3)t_{\text{sc}}$ in each test run. In order to control for this relaxation in the collision runs we place the cluster centers far enough apart initially that their cores do not interact until this amount of time has passed.

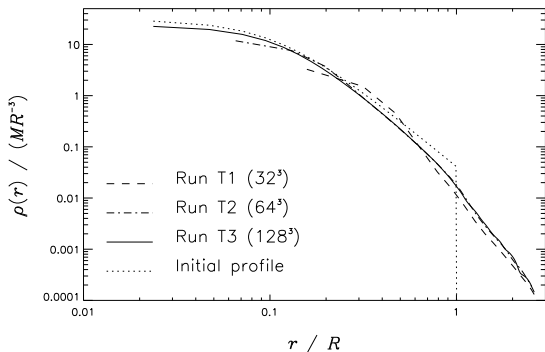


Fig. 3.— Angle-averaged density profiles in single-cluster test runs at $t = 20t_{\text{sc}}$. The dotted line indicates the initial truncated Hubble-law profile, the dashed line indicates the final profile for run T1, the dot-dashed line indicates run T2, and the solid line indicates run T3.

Figure 3 shows angle-averaged density profiles for

the three test runs at $t = 20t_{\text{sc}}$, well after each has reached a steady state. We calculate each average profile by linearly interpolating from the computational grid along 1000 randomly chosen lines emanating from the center of mass; each line is uniformly sampled in radius out to the closest external grid boundary. The percentage deviation from average of the minimum and maximum density as a function of radius is plotted for each run in Figure 4. In run T1, for which the central zone size was somewhat larger than r_c , the final profile differs substantially from the initial profile, even in the outer regions of the cluster ($2r_c < r < R$), where the density is almost a factor of two larger than in the highest-resolution run. The density profile outside the cluster has not even converged, although its logarithmic slope has. In run T2, which used a central zone size of about $0.6r_c$, the outer regions of the cluster have converged to the high-resolution result, but the density at $r \approx 2r_c$ is overestimated by a factor of 1.2, and the region inside one core radius is low by a factor of 1.7. Although this resolution does not allow study of scales smaller than r_c , it appears to be needed in order for the outer regions of the cluster to be correct. In both run T1 and run T2 the effect of poor central resolution shows up as an overestimate of the density in the zones just outside the center and an underestimate in the central zones. This effect is most likely due to errors in the central pressure and potential gradients arising from the use of a Cartesian grid, as can be seen in Figure 4. The density asymmetry in runs T1 and T2 reaches its maximum in the zones just outside the center; for run T1 this maximum is about 35%, and for run T2 it is about 12%. Outside the cluster the asymmetry increases to more than 50% in each of the runs because of the finite box size effects mentioned earlier.

The density profile in run T3, which used a zone size equal to one-fifth of a core radius, agrees with the 64^3 result outside $r \approx 2r_c$, but increases smoothly and monotonically to its central value, which is 20–30% smaller than the initial central value. This decrease

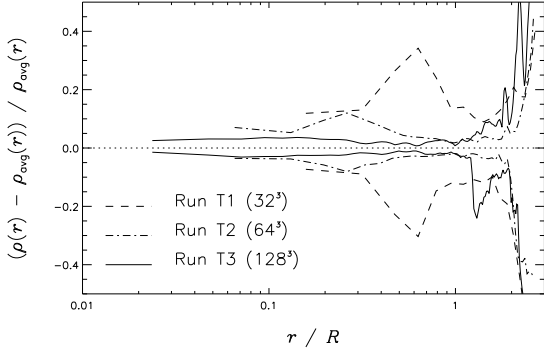


Fig. 4.— Fractional deviation from the average of the minimum and maximum density as a function of radius in the single-cluster test runs at $t = 20t_{\text{sc}}$.

in the central density is to be expected because of the initial pressure-driven expansion of the cluster, the consequent loss of 15% of the initial mass through the grid boundary, and the lack of a radiative cooling mechanism. For $2r_c \leq r \leq 8r_c$ the density drops as $r^{-3.1}$, slightly more steeply than the initial r^{-3} profile. Outside of the cluster the density drops as $r^{-4.8}$. The density asymmetry inside the cluster is everywhere less than 5%, and in the outer regions of the cluster it drops as low as 1%. Because of the average density profile’s agreement with the 64^3 result, its smoothness and monotonicity, and its spherical symmetry, we regard the 128^3 result as being adequately converged. The central zone size used in our collision runs is approximately one-third of a core radius, between the zone sizes in runs T2 and T3.

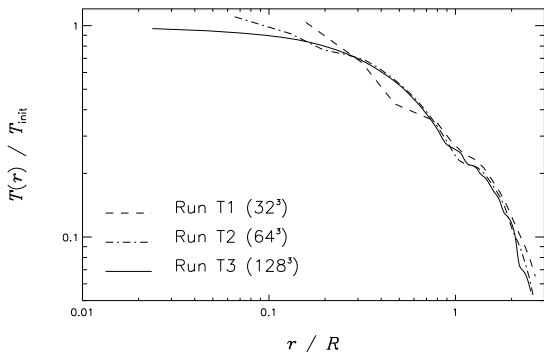


Fig. 5.— Angle-averaged temperature profiles in single-cluster test runs at $t = 20t_{\text{sc}}$.

In none of the test runs does the cluster remain isothermal. During the cluster’s initial expansion, most of the adiabatic cooling occurs in its outer regions. Figure 5 shows the angle-averaged temperature profile in each run at $t = 20t_{\text{sc}}$. The temperature at the edge of the cluster ($r = R$) has fallen by a factor of five in each run, and at the edge of the grid it is smaller again by a factor of two. The central temperature is close to its original value of unity in each case, but in runs T1 and T2 it is about 5–10% higher. This is consistent with the underestimated central density and resultant shallowness of the density profile near the center in these runs. In run T1 the temperature in the outer regions of the cluster is badly underestimated. As with the density profile, the temperature profile in run T3 increases smoothly and monotonically to its central value, 0.98. Outside of $r \approx 3r_c$ it agrees well with the result from run T2.

We conclude from these observations that resolving the core region is of great importance for minimizing numerical effects due to the Cartesian geometry of our grid. These effects include an underestimate of the central density relative to the regions just outside the center, asymmetry in the density profile just outside the center, and excessive heating of the central zones. The amount of material lost from the cluster during its expansion, and the slope of the density and temperature profiles outside the cluster, do not appear to depend significantly on the core resolution, but poor core resolution does cause an overestimate of the density and a substantial underestimate of the temperature in the regions just outside the core. A zone size smaller than $r_c/2$ for the region $r < 3r_c$ appears to be needed in order to avoid these effects.

Although we regard this resolution as adequate for the study of our nonradiating cluster gas, when comparing our results to real systems the bremsstrahlung cooling time must be kept in mind. For radii smaller than r_c the initial radiative cooling timescale,

$$t_{\text{cool}} = 2.6 \left(\frac{R}{\text{Mpc}} \right) \left(\frac{\rho}{MR^{-3}} \right)^{-1} \left(\frac{T}{T_{\text{init}}} \right)^{1/2} t_{\text{sc}}, \quad (5)$$

can be comparable to the sound crossing time. In order to correctly resolve scales smaller than this it is necessary to include radiative cooling, which in addition to permitting the study of cooling flows would tend to stabilize the cluster against the spreading caused by errors in the pressure and potential gradients.

4. Results

In this section we present results from three collision simulations using equal-mass clusters at different impact parameters: zero, five, and ten core radii. The three collisions were followed until $t = 12t_{sc}$, well beyond the point at which the merger remnant reached equilibrium in each case. The different collisions all involve multiple interacting shocks whose behavior and effect on the overall progress of the collision change with increasing impact parameter. Here we consider this variation as revealed by snapshots of the density, temperature, and velocity fields, and by the projected X-ray surface brightness and temperature fields, at several different timesteps.

4.1. Head-on collision

The first run we performed, run A, simulated a head-on collision ($b_{init} = 0$). In Figures 6a and 6b we present snapshots of the density, temperature, and velocity fields at six representative times during the simulation in the plane having a constant z -value of $1/2$ the box height. The first figure shows an $8.1R \times 8.1R$ section of the complete plane, and the second shows the innermost 16% of this region. In both plots the abscissa is the x -axis, and the ordinate is the y -axis.

These figures show several important features of the collision. Of particular interest is the contrast between the behavior of the cores and that of the outer regions of each cluster. In the first snapshot of each figure, corresponding to $t = 2t_{sc}$, the outer regions of the clusters have collided, forming a pair of slow-moving shock waves which propagate along the collision axis in both directions. Because of the clusters' gravitational potential, these shocks move more rapidly in the regions away from the collision axis, giving them a pinched appearance at the center of the grid. In the region between the shocks, the temperature is higher than its pre-shock value by about a factor of three. The approaching cluster cores compress this shock-heated gas, causing it to be expelled from the collision axis at about one-half the clusters' initial free-fall velocity. The speed of this material increases by a factor of two as it accelerates down the pressure gradient.

As the cluster cores collide at the center of the grid just before $t = 3t_{sc}$, they produce a region of greatly enhanced pressure which is out of equilibrium with the local gravitational potential. This results in

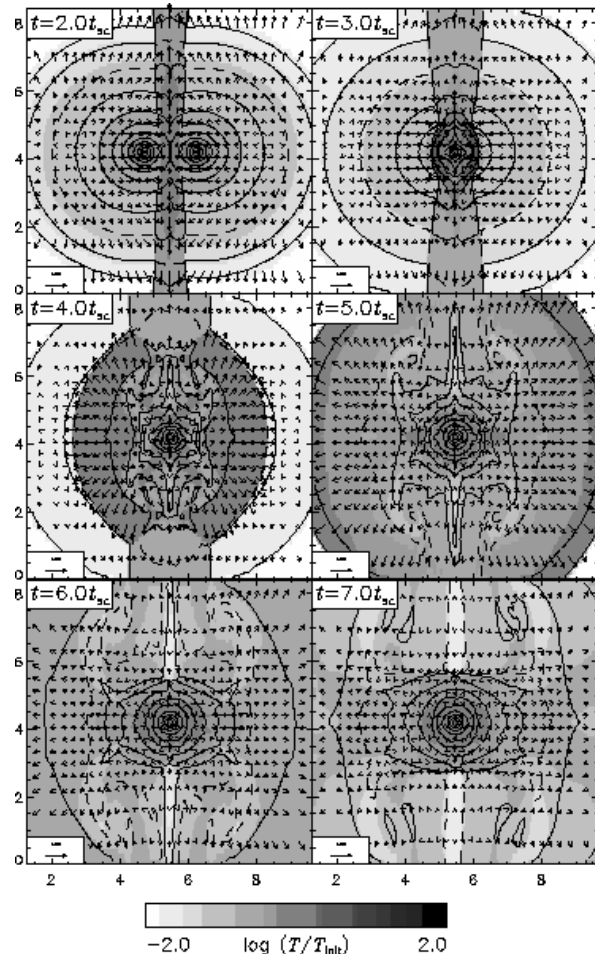


Fig. 6a.— Density and temperature snapshots for run A in the xy -plane passing through the cluster centers. Units are as described in the text, with $R = M = T_{init} = t_{sc} = 1$. Density contours are separated by a factor of three; the dashed contour indicates $\log \rho = -1$. Shading indicates the logarithm of the temperature. Velocity arrows are drawn for every eighth cell, with the fiducial arrow at the corner of each plot representing $v = 1$.

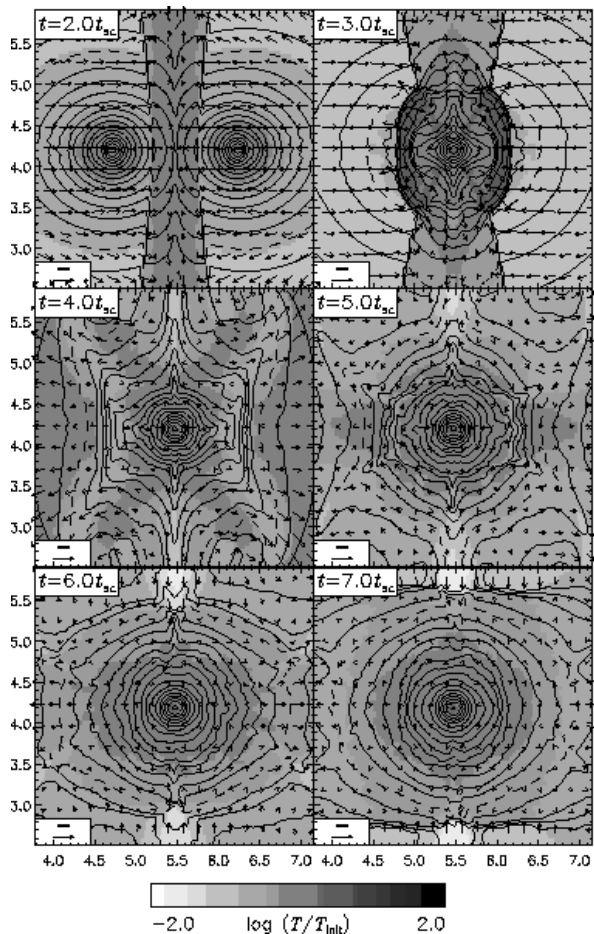


Fig. 6b.— Detail of the innermost 16% of Figure 6a (the xy -plane). Log density contours are spaced every 0.25. Velocity arrows are drawn for every sixth cell; the fiducial arrows indicate $v = 0.5$.

a rapidly expanding, roughly ellipsoidal shock wave (Mach ~ 5.5) which heats the surrounding gas, carrying away from the core the excess thermal energy resulting from the collision. This shock, which was seen also in the simulations of Schindler and Müller (1993) (who described it as ‘lens-shaped’), propagates more slowly in the region which was preheated by the initial pair of shocks, leading to a wishbone-shaped distortion in the ellipsoidal shock front. This is most clearly visible in the plots in the second row of Figures 6a and 6b, which depict the simulation at $t = 4t_{sc}$ and $t = 5t_{sc}$. At this point it has slowed by about a factor of two from its initial speed relative to the unshocked gas, but because of the temperature gradient its Mach number has increased to about 18.

In front of the ellipsoidal shock wave the initial pair of roughly planar shocks has continued to move parallel to the collision axis. Behind the ellipsoidal shock front, however, these shocks have mostly been disrupted, leaving behind a disk of relatively cold gas perpendicular to the collision axis. By $t = 5t_{sc}$ this gas has begun to fall back onto the merger remnant. The gas outside the region preheated by the initial pair of shocks (but now inside the ellipsoidal shock) has been shocked into radial motion away from the center of the grid, but is decelerating due the gravitational pull of the (now combined) cluster cores.

By $t = 6t_{sc}$ the ellipsoidal shock has left the grid, taking with it approximately 15% of the initial mass of the clusters. The material left in its wake has begun to fall back onto the merger remnant, creating a weak cylinder-shaped accretion shock. The density inside the accretion shock is settling into a roughly spherical distribution, with small fluctuations in the velocity field. The temperature at the center is slightly higher than in the regions just inside the accretion shock. As time passes this temperature difference decreases. The central density and temperature after $t = 7t_{sc}$ are roughly constant at about twice their initial values.

In Figure 7 we present projected X-ray surface brightness contour maps (integrated over the ROSAT energy band, 0.1–2.4 keV) for the merging system at four of the representative times of Figure 6a, as viewed along the x -, y -, and z -axis. For the purpose of generating these maps we have assumed a cluster mass $M = 4.4 \times 10^{14} M_{\odot}$, radius $R = 1.58$ Mpc, sound crossing time $t_{sc} = 1.5$ Gyr, and initial temperature $T_{init} = 4.5 \times 10^7$ K. The bremsstrahlung emissivity ϵ_{ff}

is given by (Rybicki & Lightman 1979)

$$\epsilon_{\text{eff}} = KI(T) \left(\frac{\rho}{MR^{-3}} \right)^2 \left(\frac{T}{T_{\text{init}}} \right)^{1/2} MR^{-1} t_{\text{sc}}^{-3}, \quad (6)$$

where, for our choices of G and μ/k ,

$$K \equiv 0.23 \left(\frac{R}{\text{Mpc}} \right)^{-1}. \quad (7)$$

We define

$$I(T) \equiv \int_{T_a/T}^{T_b/T} x^{-0.4} e^{-x} dx, \quad (8)$$

where $T_a = 0.1 \text{ keV}/h$ and $T_b = 2.4 \text{ keV}/h$ define the observing energy range. (With the ROSAT energy band, $I(T)$ is roughly constant and equal to unity for $5 \times 10^6 \text{ K} < T < 10^8 \text{ K}$.) As Schindler and Müller noted for their simulations, here we see that a favorable viewing angle is needed to detect the ongoing collision; we note also that one must observe the system within one sound-crossing time or so of the core collision to see any significant distortions in the X-ray isophotes, even for the most favorable viewing angles (along the y and z axes). During this period the isophotes in the center of the map have a distinctly oval appearance. However, despite the strength of the ellipsoidal shock, the density enhancement just behind it is not sufficient to make it even as luminous as 10^{-5} times the central luminosity. The accretion shock is also not visible. In the X-ray projections at $t = 5t_{\text{sc}}$ the cluster appears spherically symmetric and relaxed from all directions.

Projected temperature maps, weighted by the X-ray emission in the ASCA band (1.5–11 keV), are shown as grayscales in Figure 7. To generate these maps we assumed the same values for M , R , t_{sc} , and T_{init} as we used in generating the X-ray surface brightness maps. The temperature maps make it clear that, in order to see the shocks in this problem (except for the initial pair), one must look not at the X-ray surface brightness but at the X-ray temperature; all of the shocks described earlier are visible in these maps. This is true partly for the following reason. The bremsstrahlung emissivity (6) is very sensitive to the density and only weakly sensitive to the temperature. However, the Rankine-Hugoniot conditions, which relate the jumps in density, pressure, and velocity across a shock to the shock’s Mach number M relative to the pre-shock gas, limit the density

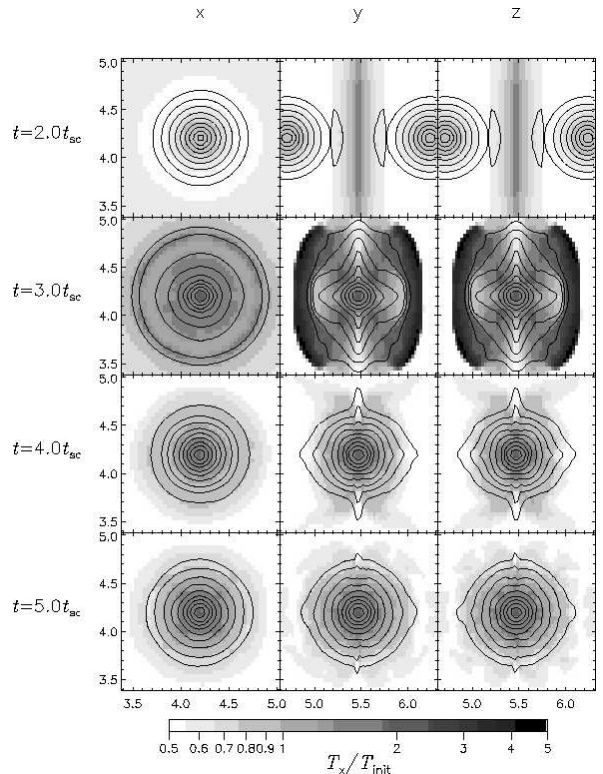


Fig. 7.— Projected maps for run A of ROSAT X-ray surface brightness (S_x) and ASCA emission-weighted temperature (T_x), viewed along the x , y , and z axes. The innermost $1.6R$ of the grid is shown. S_x (in units of $Mt_{\text{sc}}^{-3} \text{ sr}^{-1}$) is represented by contours spaced by a factor of three, with the outermost contour indicating $\log S_x = -3.5$. T_x is represented by shading.

jump across the shock to (Landau & Lifschitz 1987)

$$\frac{\rho_2}{\rho_1} = \frac{(\gamma + 1)M^2}{(\gamma + 1) + (\gamma - 1)(M^2 - 1)} \xrightarrow{M \rightarrow \infty} \frac{\gamma + 1}{\gamma - 1}. \quad (9)$$

Here ρ_1 is the pre-shock density, and ρ_2 is the post-shock density. On the other hand the temperature jump can increase without bound:

$$\begin{aligned} \frac{T_2}{T_1} &= \frac{[(\gamma + 1) + 2\gamma(M^2 - 1)]}{(\gamma + 1)^2 M^2} \times \\ &[(\gamma + 1) + (\gamma - 1)(M^2 - 1)] \quad (10) \\ &\xrightarrow{M \rightarrow \infty} \frac{2\gamma(\gamma - 1)}{(\gamma + 1)^2} M^2 \end{aligned}$$

Naively substituting the limiting density (9) and temperature (10) ratios into the expression (6) for the bremsstrahlung emissivity, we find that the limiting emissivity enhancement across a strong shock is

$$\frac{\epsilon_{\text{ff},2}}{\epsilon_{\text{ff},1}} \xrightarrow{M \rightarrow \infty} \frac{(\gamma + 1)^{2.2}}{(2\gamma)^{0.1}(\gamma - 1)^{2.1}} J(T_1) M^{-0.1}, \quad (11)$$

where

$$J(T_1) \equiv \frac{1}{I(T_1)} \int_{T_a/T_1}^{T_b/T_1} dx x^{-0.4} = \frac{T_b^{0.6} - T_a^{0.6}}{0.6 T_1^{0.6} I(T_1)} \quad (12)$$

is a weak function of the pre-shock temperature. Hence X-ray emissivity (even without projection effects) is a much poorer detector of strong planar shocks than gas temperature. It should be noted, however, that this result is only valid at large distances from the center of the cluster potential.

4.2. $b_{\text{init}} = 5r_c$

Run B was the first off-center collision, with impact parameter $b_{\text{init}} = 5r_c$. Figures 8a and 8b show snapshots of the density, temperature, and velocity in this run for 100% and the innermost 16%, respectively, of the midplane perpendicular to the z -axis (the collision plane). Once again the abscissa in these plots is the x -axis, and the ordinate is the y -axis. Figure 8c gives a zoomed view of the midplane perpendicular to the y -axis; here the ordinate is the z -axis.

In this run, as in the head-on case, we see a sequence of initial planar shocks, followed by a fast ellipsoidal shock as the cores collide, followed by an accretion shock as material falls back onto the merger

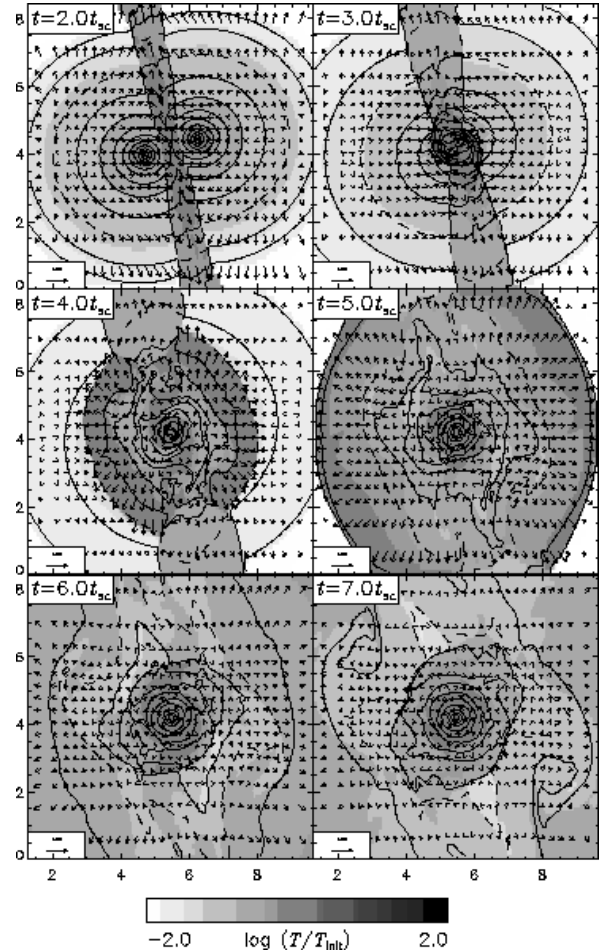


Fig. 8a.— Slices of log density and log temperature for run B, taken perpendicular to the z -axis through the center of the box. Units, ranges, and contour spacing are as in Figure 6a.

remnant. However, the behavior of these shocks is more complex, and the presence of angular momentum in the system alters their roles somewhat. The cluster cores survive intact longer, and the merger remnant requires more time to reach equilibrium.

The planar shocks produced by the clusters' initial interaction (seen at $t = 2t_{sc}$) are now oblique, making a $\sim 72^\circ$ angle with the collision axis. The temperature jump and outflow velocity in the post-shock region are comparable to the values in run A.

As previously noted, in the off-center runs the cluster cores survive intact beyond the time at which they would have merged in the head-on case. The size of each core is determined roughly by the ram pressure of the gas through which it passes: the cluster remains intact where its own gas pressure exceeds the ram pressure. As we increase the impact parameter of the collision, the density ρ' of the gas through which each core must pass decreases rapidly, while the relative speed v remains roughly the same. The core's gas pressure p decreases with radius in the same way that ρ' decreases with b_{init} . Therefore the radius at which p drops below the ram pressure ($\sim \rho'v^2$) should be roughly proportional to b_{init} . The sizes of the cluster cores seen in runs B and C are consistent with this explanation.

Because the planar shocks are now oblique they play a new dynamical role not found in the head-on collision. The cluster cores, defined as described above, carry most of the angular momentum and survive past the point at which they would have coalesced in the head-on case. The cores are not disrupted by the planar shocks; instead each passes through the shock which propagated toward it, then drives the other shock ahead of it, so that the central part of each planar shock is twisted into a spiral pattern. As each core moves through the outer regions of the other cluster, it creates a strong, curved bow shock which propagates out of the center of the grid. Together these form a fast ellipsoidal shock front similar to (but weaker than) that created by the core collision in the head-on case. This shock serves to dissipate the excess kinetic energy of the cluster cores, enabling them to fall into orbit about one another. However, not all of the excess is carried away by this shock; the remainder is dissipated more slowly by what is left of the slower, originally planar shocks ($t = 3t_{sc}$). By turning the material passing through them, these spiral shocks gradually transfer the orbital angular momentum of each core to the

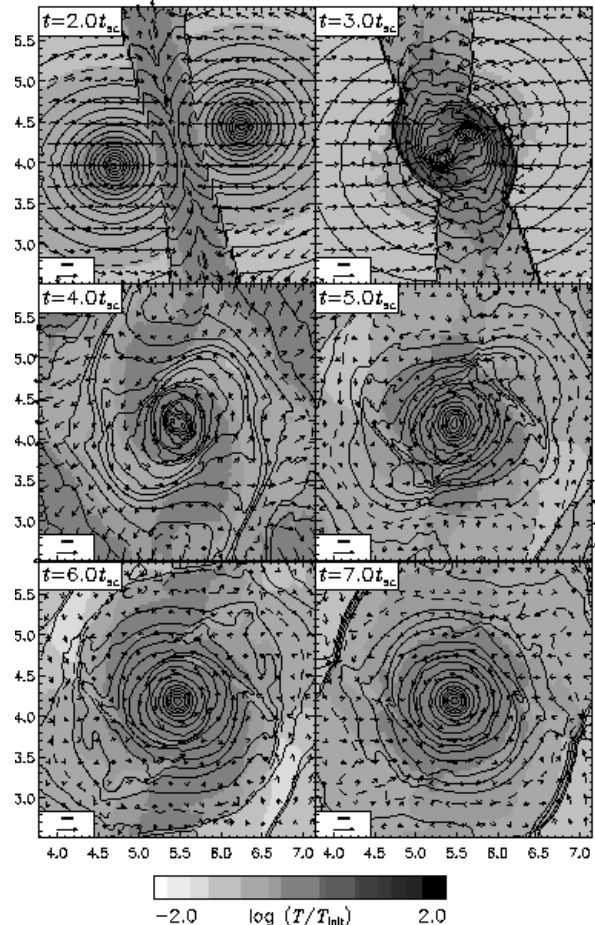


Fig. 8b.— Detail of the innermost 16% of Figure 8a (the xy -plane). Units, ranges, and contour spacing are as in Figure 6b.

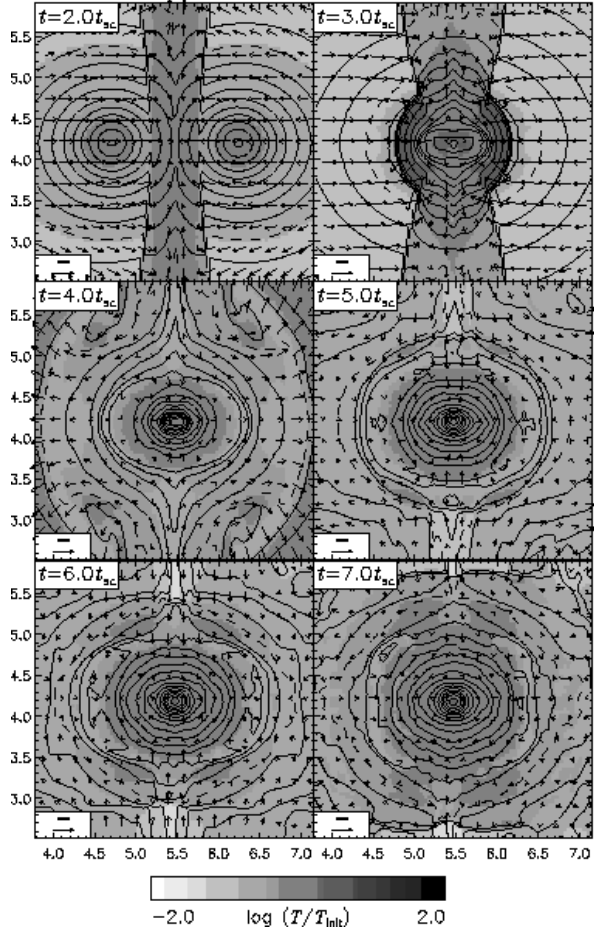


Fig. 8c.— Slices of log density and log temperature for run B, taken perpendicular to the y -axis through the center of the box. Detail of the innermost 16% of the grid is shown. Units, ranges, and contour spacing are as in Figure 6b.

surrounding low-density gas. Shortly after $t = 4t_{sc}$ the cores lose enough angular momentum in this way to fall almost directly in toward each other, having completed nearly a full revolution.

By $t = 5t_{sc}$ the ellipsoidal shock has nearly left the grid, and the gas in its wake has begun to fall back onto the merger remnant, forming an accretion shock. By $t = 7t_{sc}$ this accretion shock is fairly well-developed and lies roughly $1.5R$ from the center of the remnant. The remnant itself is rotating, and weak spiral shocks (the remains of the twisted planar shocks described earlier) can be seen; these are completing the redistribution of angular momentum out of the cluster cores. By $t = 7t_{sc}$ the merger remnant has relaxed to a roughly ellipsoidal shape and is rotating about the z -axis. A small amount of density substructure is still present in the innermost part of the remnant ($r < r_c$) at this time, although on this scale the core of the remnant appears to be isothermal.

The projected ROSAT X-ray surface brightness for run B (contours in Figure 9) shows a clearly separated double-peak structure while the cluster cores are orbiting one another. The bending of the planar shocks is also visible. After the cores collide at $t \sim 4t_{sc}$, the bimodal structure disappears, but the X-ray isophotes continue to appear significantly distorted, forming a barlike structure which rotates about the z -axis. When viewed along the bar, the cluster appears roughly spherical, and when viewed off-axis in the plane of the bar's rotation, the cluster appears elliptical, with the major axes of the isophotes roughly parallel. It is only when the cluster is viewed from well outside the plane of the bar's rotation that the differing ellipticities and angles of orientation of the isophotes reveal the ongoing equilibration of the cluster. However, this cluster continues to appear aspherical from some directions long after the cluster formed in the head-on case has ceased to show any detectable evidence of a collision.

The projected ASCA-weighted temperature for this run (grayscale in Figure 9) shows much clearer evidence for an off-center collision, but after the cores have collided this also requires a favorable viewing angle. As in the head-on case, a hot bar-shaped structure is present in the temperature maps. However, here it is perpendicular to the line connecting the cluster cores, not to the initial collision axis.

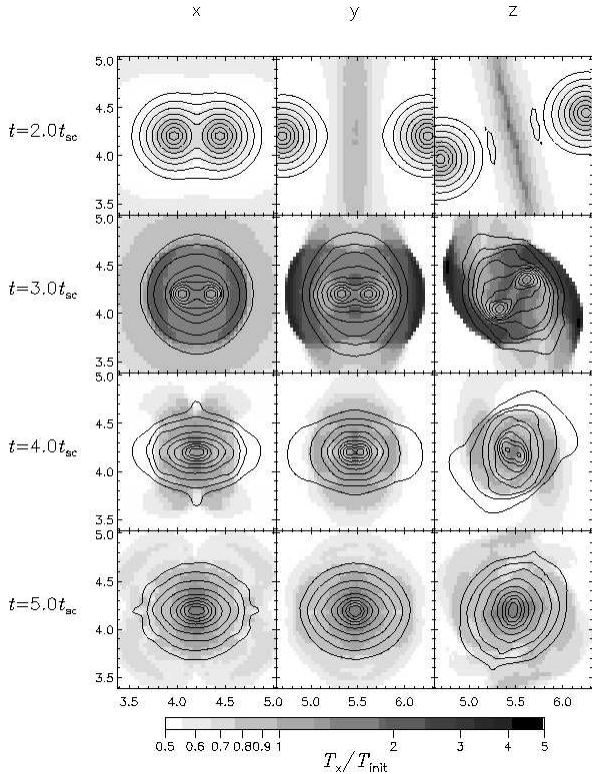


Fig. 9.— Projected maps for run B of ROSAT X-ray surface brightness (S_x) and ASCA emission-weighted temperature (T_x), viewed along the x , y , and z axes. The innermost $1.6R$ of the grid is shown. S_x (in units of $Mt_{sc}^{-3}\text{sr}^{-1}$) is represented by contours spaced by a factor of three, with the outermost contour indicating $\log S_x = -3.5$. T_x is represented by shading.

4.3. $b_{\text{init}} = 10r_c$

In Run C we used an impact parameter $b_{\text{init}} = 10r_c$. For this run, Figures 10a and 10b show full and zoomed snapshots of the midplane perpendicular to the z -axis (the collision plane). Figure 10c gives a zoomed view of the midplane perpendicular to the y -axis. This run displays many of the same qualitative features as the $b_{\text{init}} = 5r_c$ case. However, while the collision itself is more violent, and the merger remnant requires much longer to relax to a new equilibrium configuration, the release of kinetic energy is much more gradual.

The initial interaction of the clusters' outer regions again forms a pair of planar shocks, now at a $\sim 54^\circ$ angle with the collision axis. Because of their greater obliqueness they do not begin to twist until much later

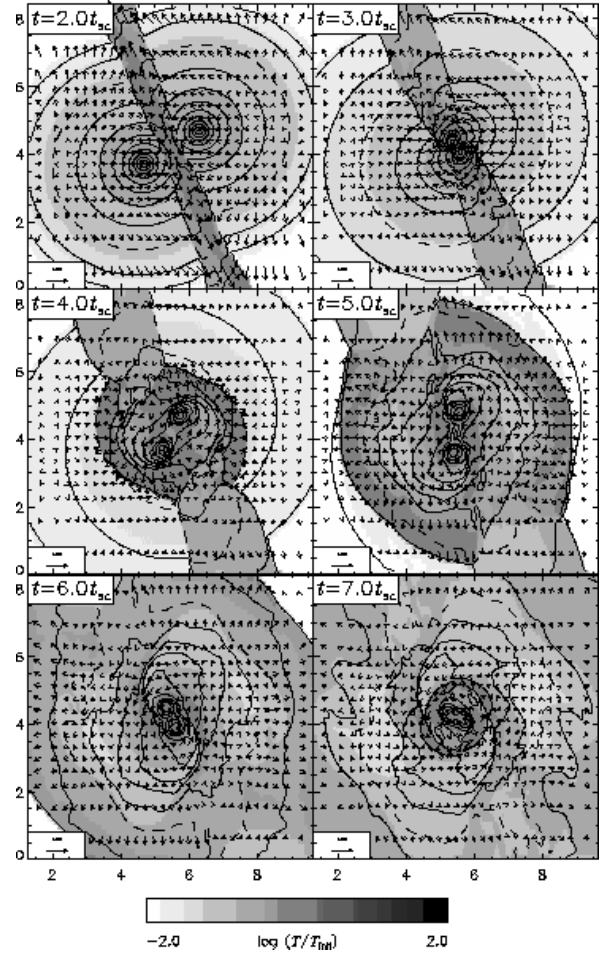


Fig. 10a.— Slices of log density and log temperature for run C, taken perpendicular to the z -axis through the center of the box. Units, ranges, and contour spacing are as in Figure 6a.

than in run B, and they brake the cluster cores and transfer their angular momentum to the surrounding gas less efficiently. The ellipsoidal shock which allows the cores to remain bound to each other does not form until just after $t = 3t_{sc}$. In this run it dissipates a smaller fraction of the cores' initial energy than in the other two cases. A larger fraction of this energy is dissipated by the spiral shocks which are driven by the cores as they orbit each other. The cores complete about $1\ 1/2$ orbits in the process of spiraling in toward each other; they do not merge until $t = 6.5t_{sc}$. The size of the cores themselves is much larger (diameter $\sim 8r_c$ vs. $\sim 5r_c$ for $b_{\text{init}} = 5r_c$), supporting the idea that their size is determined by ram pressure.

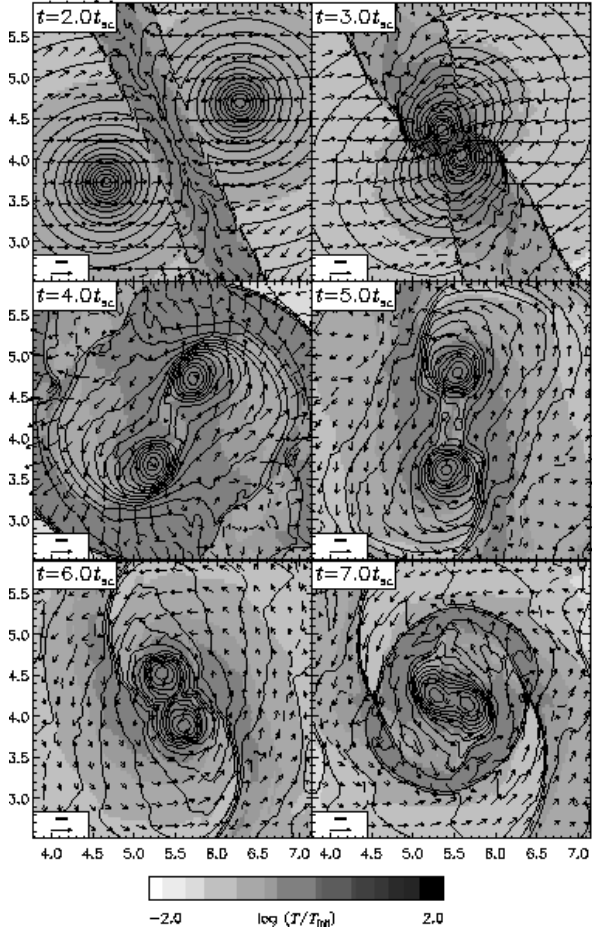


Fig. 10b.— Detail of the innermost 16% of Figure 10a (the xy -plane). Units, ranges, and contour spacing are as in Figure 6b.

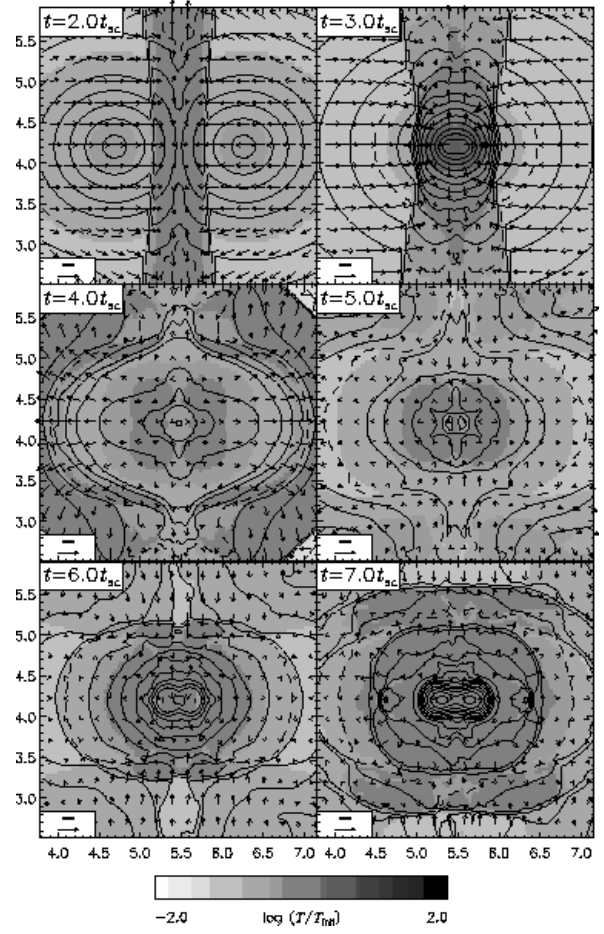


Fig. 10c.— Slices of log density and log temperature for run C, taken perpendicular to the y -axis through the center of the box. Detail of the innermost 16% of the grid is shown. Units, ranges, and contour spacing are as in Figure 6b.

The projected ROSAT X-ray emission for this run (contours in Figure 11) shows significantly more evidence for an ongoing merger than in the other two runs. Bimodal structure is present in the X-ray maps well past $t = 5t_{\text{sc}}$. In the projected ASCA emission-weighted temperature maps (grayscale in Figure 11), bimodal structure also persists past $t = 5t_{\text{sc}}$. The bow shocks are easily visible at $t = 4t_{\text{sc}}$ and $5t_{\text{sc}}$. From above the plane of the bar's rotation, some evidence of spiral structure can be seen at $5t_{\text{sc}}$.

5. Discussion

In this section we compare the three collision runs described in the previous section in terms of the time required for each to relax to its final equilibrium state, the increase in X-ray luminosity during the collision, and the structure of the merger remnant.

5.1. Equilibration time

In hierarchical models of large-scale structure formation, clusters of galaxies form through a series of mergers followed by periods of relaxation. How relaxed clusters look in such a model at any given time depends on the ratio of the equilibration time to the average interval between mergers. If this ratio is much larger than one, so that, on average, clusters have not completely assimilated the effects of one merger before the next takes place, clusters will not appear to be in equilibrium. If the opposite is true, so that the equilibration time is much smaller than the merger interval, then clusters will usually appear to be virialized, even if the merger rate is quite high. The fraction of clusters which appear to be far from equilibrium therefore is telling us something about this ratio.

The rate at which mergers take place depends on the assumed underlying cosmological model, while the average equilibration time consists of two factors: the equilibration time for mergers having particular values of the impact parameter, relative velocity, and relative mass, and the distribution of mergers with these parameters as a function of cosmological parameters. The first factor is presumably only weakly dependent on cosmology, since the relaxing region has detached itself from the general cosmic expansion; the second depends on the tidal torques generated in different models. If we are to reason backward from the fraction of clusters which appear unrelaxed and the rate at which clusters are observed to merge to de-

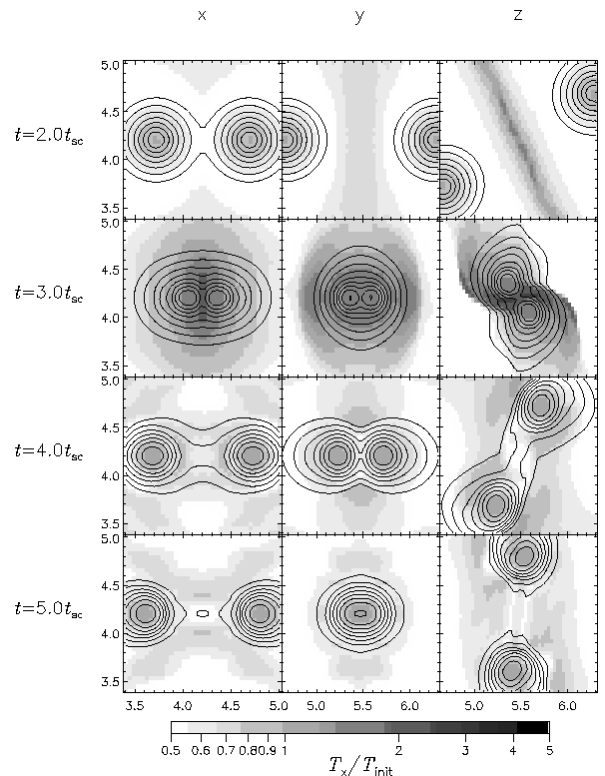


Fig. 11.— Projected maps for run C of ROSAT X-ray surface brightness (S_x) and ASCA emission-weighted temperature (T_x), viewed along the x , y , and z axes. The innermost $1.6R$ of the grid is shown. S_x (in units of $Mt_{\text{sc}}^{-3} \text{sr}^{-1}$) is represented by contours spaced by a factor of three, with the outermost contour indicating $\log S_x = -3.5$. T_x is represented by shading.

duce the underlying cosmological model (as specified by Ω_0 , Λ , etc.), we need to understand the physical factors influencing the equilibration rate for collisions with given parameters.

While our present simulations concern themselves only with the behavior of the gaseous component of galaxy clusters, thus ignoring the effect on the equilibration rate of energy transfer between the gas and the dark matter, we can nevertheless draw some conclusions regarding the rate of equilibration after an off-center merger.

Physically motivated definitions for the equilibration time will differ markedly from those based on observational criteria; furthermore, physically motivated definitions based on average quantities will differ from those based on the actual presence of substructure (regardless of whether this is observable or not). In general we find that observational criteria (such as the projected luminosity and temperature maps described in the previous section) lead to shorter equilibration times than criteria based on the degree of virialization of the merger remnant.

From an observational standpoint the time required in our simulations for the merging clusters to reach a new equilibrium state is short. The projected X-ray surface brightness (Figures 7, 9, and 11) shows little evidence of the shocks which are produced in each run. The high density of material in the cluster cores' gravitational wells accounts for most of the X-ray emission, and what evidence exists in the X-ray maps for an ongoing merger, such as bimodality, is only present when the cores are well-separated in the plane of the sky, or when they have not yet fully coalesced. This is partly due to projection effects and partly because the bremsstrahlung emissivity poorly delineates planar shocks.

In the head-on case bimodality is only present before the collision; after the collision the anisotropy caused by material falling back onto the remnant perpendicular to the collision axis is only visible for about one sound crossing time. In the case of $b_{\text{init}} = 5r_c$ the cores do not coalesce as rapidly; consequently they are distinguishable both before the collision and for more than one sound crossing time after the ellipsoidal shock front forms. During this time they are orbiting one another, and they only appear well-separated if viewed from above the orbital plane or if, by chance, they are viewed at a point in their orbit when neither lies in front of the other. However, from all directions the X-ray isophotes remain fairly ellipti-

cal, with an axial ratio of approximately 2:1, until several sound crossing times have passed. When viewed in the collision plane the long axes of the isophotes are all oriented in the same direction, parallel to the collision plane. When viewed from above the collision plane, their axes are not aligned; the innermost contours are advanced in the direction of rotation relative to the outermost ones. Initially the difference in angle is as large as 90° , but this decreases with time. By $t = 5t_{\text{sc}}$ the difference has decreased to 45° , and at late times the remnant appears spherically symmetric. Thus the rotation of the merger remnant in run B does not appear to significantly affect the shape of the X-ray isophotes at late times. The case of $b_{\text{init}} = 10r_c$ displays many of the same characteristics as that of $b_{\text{init}} = 5r_c$ prior to the final merging of the cluster cores, except that the cores' inspiral requires more than three crossing times, allowing bimodal structure to be visible substantially longer than in runs A and B.

The virial theorem provides a useful physical criterion for determining when the system is close to equilibrium. Whether the system is relaxed or not, the virial theorem requires that

$$\frac{1}{2} \frac{d^2 I}{dt^2} = 2T + W + 3(\gamma - 1)U \quad (13)$$

(Chandrasekhar 1961), where I is the moment of inertia and T , W , and U are the total kinetic, potential, and thermal energies, respectively:

$$\begin{aligned} I &\equiv \frac{1}{2} \int d^3x \rho(\mathbf{x}) |\mathbf{x}|^2 \\ T &\equiv \frac{1}{2} \int d^3x \rho(\mathbf{x}) |\mathbf{v}(\mathbf{x})|^2 \\ W &\equiv -\frac{1}{2} G \int \int d^3x d^3x' \frac{\rho(\mathbf{x})\rho(\mathbf{x}')}{|\mathbf{x} - \mathbf{x}'|} \\ U &\equiv \frac{1}{\gamma - 1} \int d^3x p(\mathbf{x}) . \end{aligned} \quad (14)$$

The volume integrals in these definitions are taken over the entire grid. When the system has reached a steady state, the left-hand side of equation (13) will be zero. We can approximate this criterion for practical purposes by dividing equation (13) by W :

$$\left| \frac{1}{2W} \frac{d^2 I}{dt^2} \right| = \left| 2 \frac{T}{W} + 1 + \frac{3(\gamma - 1)U}{W} \right| < \epsilon \ll 1 . \quad (15)$$

When this criterion is satisfied for some suitably chosen value of ϵ , the system will be close to equilibrium.

In Figure 12 we have plotted the second expression in equation (15) as a function of time for the three runs. We set ϵ to 0.02, roughly the level of round-off error in our determination of T , U , and W , and roughly the point at which the virial parameter becomes constant in these runs. Although during the period following the collision the behavior of the energy in run A differs substantially from that in run B, both runs reach equilibrium according to our criterion approximately $5t_{\text{sc}}$ after the initial core interaction (represented by the initial peak for each curve). Run C, in contrast, requires more than $6t_{\text{sc}}$ to reach equilibrium after the initial core interaction. The virial parameter in this case passes through several maxima, reflecting the strength of the second and subsequent core interactions.

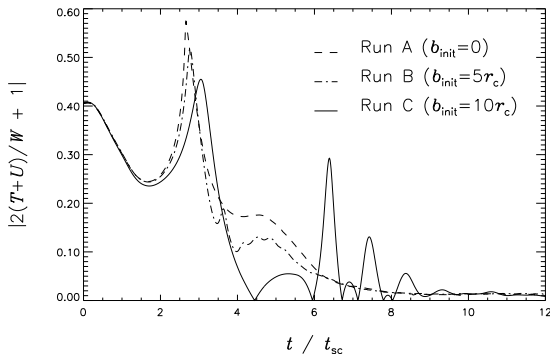


Fig. 12.— Factor by which the colliding clusters depart from virial equilibrium as a function of time for the three collision runs.

Using observational criteria to determine equilibration time, we see that off-center collisions can take substantially longer than head-on collisions to reach a new equilibrium state. The virial equilibration time is less sensitive to the impact parameter but is at least twice the observational equilibration time. Given typical sound crossing times $t_{\text{sc}} \sim 1$ Gyr, both the observational and the virial equilibration times can be a substantial fraction of the age of the universe.

Adding collisionless dark matter to our simulations would tend to increase the equilibration time, since the dark matter does not experience shocks and so must dissipate its initial kinetic energy through violent relaxation and drag due to the baryonic contribution to the potential. Adding radiative cooling would tend to decrease the equilibration time some-

what by permitting the gas in the cluster cores to radiate away some of the kinetic energy in excess of the potential energy available to bind the cores, leading to weaker shocks during the collision. However, the cooling time is typically very long outside the cluster cores, so cooling should not affect the dynamics of these regions very much. In the central region where the cooling time is relatively short, the timescale for production of the ellipsoidal shock, which dissipates most of the cores' energy, is also short. Therefore it is likely that radiative cooling will have a much smaller effect on the equilibration timescale than it will have, for instance, on the luminosity of the clusters during the collision or the density and temperature profiles of the merger remnant.

5.2. Brightening during the collision

During the course of each collision the X-ray luminosity of the system varies significantly. The effect of changing the impact parameter on this luminosity evolution can be seen in Figure 13, which shows as a function of time the total energy loss rate, integrated over all frequencies, due to bremsstrahlung emission in each of the collision runs. This is just the total X-ray luminosity as a function of time:

$$L_x = 1.49K \sum_{ijk} \frac{\Delta V_{ijk}}{R^3} \left(\frac{T_{ijk}}{T_{\text{init}}} \right)^{1/2} \left(\frac{\rho_{ijk}}{MR^{-3}} \right)^2 MR^2 t_{\text{sc}}^{-3}. \quad (16)$$

Before $t = 1.5t_{\text{sc}}$ the luminosity drops by about one-third due to the adiabatic cooling related to our initial conditions, as discussed in Section 3. Near $t = 3t_{\text{sc}}$, when the ellipsoidal shock forms in each run, the radiative energy loss rate increases briefly by as much as a factor of 50, then drops to a new constant level 4–5 times its lowest pre-collision value. The height and width of the luminosity peak indicate the amount and duration of the compression experienced by the intra-cluster gas as the cluster cores approach one another. Thus in the head-on case we see one tall peak lasting about $t_{\text{sc}}/2$, while in run B the initial peak is about one-third as tall and is followed by several smaller peaks as the cluster cores spiral inward toward one another. In run C the cores orbit several times before coalescing; hence we see several peaks, with the luminosity following each peak gradually increasing to roughly the same final level as in runs A and B. Because of the long duration of the first orbit in run C, the second and subsequent luminosity peaks in this case appear about $3t_{\text{sc}}$ after the first peak.

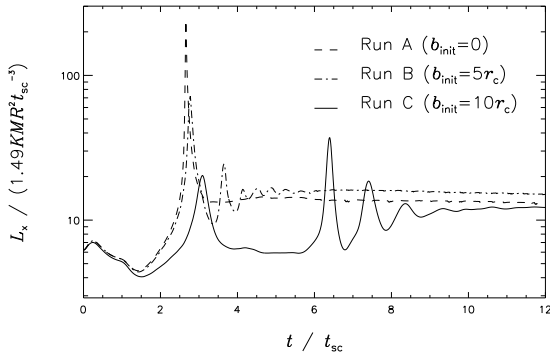


Fig. 13.— Radiative energy loss rates due to bremsstrahlung emission for the three collision runs (were cooling included).

Because we do not include radiative cooling in our simulations, our luminosity enhancements are much greater than, for example, in the simulations by Schindler and Müller (1993). Nevertheless the results in Figure 13 provide information about the strength of the shocks produced in each run which should carry over to simulations which do include cooling. Our observations suggest that magnitude-limited surveys of galaxy clusters will be subject to a selection effect based on merging activity, and in particular to one based on impact parameter. Head-on mergers produce stronger shocks and are more luminous than off-center mergers. Mergers are much more visible for a relatively short time while the cluster cores are first interacting than either before or after this time. Because mergers in progress can be much more luminous than quiescent clusters, we may be overestimating the amount of merging activity at high redshift. Alternatively, since projection effects can hide isophotal evidence for mergers at most orientations, we may observe merging systems as highly luminous, apparently relaxed clusters.

5.3. Structure of the merger remnant

For all three runs we were able to follow the progress of the collision until well after the merger remnant became virialized. In this section we compare the angle-averaged density and temperature profiles in each run at $t = 12t_{\text{sc}}$. We also examine the rotation of the remnant in runs B and C at $t = 12t_{\text{sc}}$.

In Figure 14 we plot using solid lines the angle-averaged density profiles for runs A, B, and C at $t =$

$12t_{\text{sc}}$. To determine the effect of core heating on the structure of the merger remnant, we have fitted the average profiles for $r < 2R$ using two models: the β -model (Cavaliere & Fusco-Femiano 1976),

$$\rho_{\beta}(r) = \frac{\rho_0}{[1 + (r/r_c)^2]^{3\beta/2}}, \quad (17)$$

and the analytical approximation to the de Vaucouleurs (1948) model for elliptical galaxies described by Hernquist (1990),

$$\rho_H(r) = \frac{M_H a_H}{2\pi} \frac{1}{r (r + a_H)^3}. \quad (18)$$

In Figure 14 the best-fit β -model profiles are shown as dashed lines, and the best-fit Hernquist profiles are shown as dot-dashed lines. The parameters corresponding to these fits appear in Table 2. Note that the initial density profile for each cluster (equation 1) corresponds to a β -model profile with $\beta = 1$.

Strictly speaking, the β -model is intended to describe the distribution of gas which is in equilibrium with a potential determined by a collisionless matter component, such as galaxies or dark matter; the value of β then gives the ratio of the velocity dispersion of the collisionless component to the temperature of the gas. Here we have no collisionless component, so β serves more as an indicator of deviations from an isothermal distribution and as a measure of differences in core radius and central density among the runs. In particular, we expect shock heating during a collision to lead to a merger remnant with a core radius larger than that of the original clusters.

The Hernquist model, in contrast to the β -model, diverges as $r \rightarrow 0$, and at large r it drops as r^{-4} , whereas fitting with the β -model allows the slope at large r to vary. Because of our grid resolution and initial cluster profiles we do not expect the Hernquist model to give a good fit near $r = 0$, but fitting with it does allow us to check the asymptotic density slope independently of the shape of the density profile at small r . The asymptotic slope is of interest because N -body simulations of halo formation in cold dark matter (CDM) universes (proceeding, as it does in such models, through mergers) have yielded differing values for the slope. Methods neglecting infall from large scales, such as that used by Dubinski and Carlberg (1991) in studying halo formation in CDM and that used by Hernquist (1992, 1993) in simulations of galaxy mergers, produce remnants with asymptotic profiles proportional to r^{-4} . Others (e. g. Navarro,

Table 2: Best-fit β -model and Hernquist model parameters for collision runs at $t = 12t_{\text{sc}}$. The first line gives β -model parameter values for each cluster at $t = 0$. Note that the best-fit values for run C do not provide a satisfactory fit.

Run	β -model		Hernquist model		
	ρ_0/MR^{-3}	r_c/R	β	M_H/M	a_H/R
original	30.5	0.111	1.00	—	—
A	48.2	0.142	1.27	1.60	0.184
B	60.6	0.119	1.19	1.69	0.205
C	56.9	0.0904	1.02	1.74	0.304

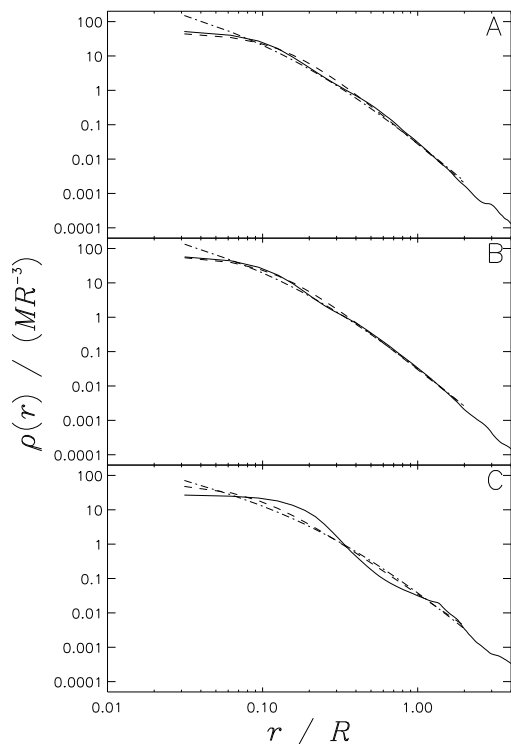


Fig. 14.— Angle-averaged density profiles, taken about the center of mass, for the merger remnants in runs A, B, and C at $t = 12t_{\text{sc}}$. The average profiles are plotted as solid lines. Best-fit model profiles described in the text include the β -model (dashed lines) and the Hernquist model (dot-dashed lines).

Frenk, & White 1996) have argued for an r^{-3} dependence on the basis of simulations which do include infall. Our calculations differ from these in that we only include collisional matter and we impose an initial profile with r^{-3} asymptotic behavior. However, like Dubinski and Carlberg we implement a vacuum boundary, neglecting infall. If hydrodynamical effects are weak at large radius, we may therefore be able to check their results. In our single-cluster tests (Section 3) we find that the asymptotic slope resulting from our artificial density cutoff at $r = R$ (which would not be needed if we could include infall) is $r^{-4.8}$, much steeper than r^{-3} or r^{-4} , whereas the slope inside the cutoff radius remains close to r^{-3} . We may therefore expect that any change to an r^{-4} profile in our simulations is an effect of the collision and not of the initial conditions.

In examining Figure 14 and Table 2, we find that in none of the runs is the merger remnant isothermal; instead, the density profile in each case drops off more steeply than the initial profile at large radii. In runs A and B the profile for $r > 0.4R$ is well-fit by the β -model with similar values of β . For $r < 0.4R$ the β -model produces a slightly poorer fit. As expected, the Hernquist model gives a poor fit for $r < 0.2R$; but at large radii both the β -model and the Hernquist model give good fits, with the best-fit value of β consistent with asymptotic slopes of 4.0 and 3.8 for runs A and B, respectively, in agreement with the results of Hernquist (1992, 1993) and Dubinski and Carlberg (1991). For run C we were unable to obtain a statistically reasonable fit with either function; the density profile in this case is characterized by a large core (ρ drops to 1/2 its central value near $r = 0.16R$), and while there is some evidence of power-law behavior outside the core, the logarithmic slope appears to

converge slowly. In all cases the density profile is consistent with an increased core radius. In runs A and B we see a large increase of the central density of the merger remnant in comparison with the central densities in the original clusters, while in run C the central density is slightly smaller than the initial value.

These results suggest that collisions with modestly varying impact parameter will produce merger remnants with substantially similar density profiles varying as r^{-4} (if infall is neglected) at large radii, while the varying amount of shock heating in such collisions will primarily manifest itself in modest differences in the core radius. Most of the mass difference between the final merger remnant and each of the initial clusters goes into a large increase in the central density. A very large impact parameter, on the other hand, results in a significantly larger core with a more complicated asymptotic profile. In such cases the transfer of angular momentum out of the remnant core by spiral shocks (as discussed in Section 4) may not be efficient enough to produce a remnant whose structure is independent of b_{init} .

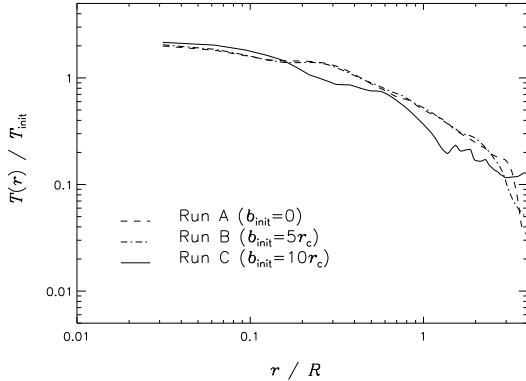


Fig. 15.— Angle-averaged temperature profiles, taken about the center of mass, for the merger remnants in runs A, B, and C at $t = 12t_{\text{sc}}$.

The angle-averaged temperature profiles for the three runs at $t = 12t_{\text{sc}}$, plotted in Figure 15, are consistent with these conclusions. For $r < 2R$ the temperature profiles in runs A and B are virtually identical, with run C slightly hotter than the other two for $r < 0.1R$ and substantially cooler outside this radius. Inside $r = 0.2R$ the temperature in runs A and B is roughly constant, dropping from a central value of $2T_{\text{init}}$ to about $1.5T_{\text{init}}$. Outside this radius the

temperature drops approximately as r^{-1} . It is interesting that the merger remnants in runs A and B are so similar; in the latter case the gas inside $r = 0.3R$ is rotating about the center of mass at an azimuthal velocity of about $0.5Rt_{\text{sc}}^{-1}$, but rotation in this case does not contribute much to its support against gravity. For $b_{\text{init}} = 10r_c$, however, the rotation of the remnant has a very significant effect on both the density and temperature profiles, suggesting that if such extreme collisions occur at all, some evidence for them will be present in the structure of the merger remnant.

6. Conclusions

We have used a new hydrodynamical code based on PPM and a multigrid isolated potential solver to study the behavior of intracluster gas in controlled collisions between equal-mass galaxy clusters at different impact parameters. A summary of our findings follows. Because of the lack of a collisionless component and of radiative cooling in our calculations, as well as the simplified initial conditions, these conclusions should not be applied to specific clusters or cosmological models. Rather the physical insight suggested by these calculations concerning the behavior of self-gravitating gas spheres should be used to aid in the interpretation of more detailed calculations which include dark matter and radiation or which use more realistic initial conditions. The isolated potential solver we have developed for these calculations is an important new component of a code we will use to perform more realistic calculations in the near future.

Three main sets of shocks affect the progress of off-center mergers between clusters of equal mass. A pair of roughly planar shocks forms through the compression of the clusters' outer regions as they approach one another. These shocks bound a disk-shaped outflow at a varying angle to the collision axis. In off-center collisions, these planar shocks become twisted into a spiral pattern through interaction with the cluster cores. The ram pressure acting on each cluster determines the size of the cluster's core. The cores drive a strong, roughly ellipsoidal shock into the outer regions of the clusters, dissipating enough energy to permit themselves to fall into orbit about one another. In the wake of this shock the cluster cores drive two curved bow shocks which gradually transfer the angular momentum of the cores to the surrounding gas as they spiral inward. After the cores collide, these spiral shocks continue to redistribute the angular momen-

tum and energy of the cores within the merger remnant. Material from the outer regions, heated and driven outward by the ellipsoidal shock front, then begins to fall back onto the merger remnant, creating a weak accretion shock. The Mach numbers of all of the shocks are modest. While the ellipsoidal and accretion shocks have been seen in previous calculations of head-on mergers between clusters of galaxies (e. g. Schindler & Müller 1993), we only observe the spiral shocks in off-center mergers. We do not observe a high-velocity, ordered flow like that seen in the calculations of Roettiger et al. (1993). This is most likely because of the low initial velocity and the lack of dark matter in our calculations.

We find that both a physical criterion for equilibrium based on the virial theorem and the presence of readily observable bimodal or elliptical structure in the projected X-ray surface brightness and emission-weighted temperature lead to equilibration times which are a significant fraction of the age of the universe, given typical sound-crossing times of ~ 1 Gyr. The virial equilibration time can be as large as 5–6 crossing times, while isophotal structure is erased within 1–2 crossing times after the initial core interaction for $b_{\text{init}} = 0$ and $b_{\text{init}} = 5r_c$. For $b_{\text{init}} = 10r_c$ the X-ray surface brightness shows evidence of structure for several crossing times due to the protracted inspiral of the cluster cores in this case. The head-on collision produces a much larger increase in brightness during the collision than the other two cases, but it is more short-lived; the luminosity enhancement due to the collision lasts about one-half of a crossing time.

The angle-averaged density and temperature profiles of the merger remnant show very little variation between a head-on collision and an off-center collision with an impact parameter equal to five times the core radius. The core radius increases slightly from its initial value due to shock heating during the collision, and the central density and temperature finish with values about twice their initial values. The central $0.2R$ of the remnant is roughly isothermal; outside this radius the temperature drops as $1/r$. Outside the core the density drops steeply, with a β value of 1.2 – 1.3, corresponding to an asymptotic behavior closer to r^{-4} than to r^{-3} . Although the merger remnant rotates in the off-center case, the remnant does not appear to be rotationally supported. For an impact parameter of ten core radii, however, the remnant is characterized by a large core, a low central density,

and a complicated profile at large radius, suggesting that the outward transfer of angular momentum by spiral shocks is inefficient in this case.

The author would like to thank Don Lamb and Craig Sarazin for advice and support during the completion of this work, and Bruce Fryxell, Scott Dodelson, Kevin Olson, and Peter MacNeice for useful and stimulating discussions. This work was primarily supported by a NASA GSRP Fellowship (NGT-51322). Some work was also supported under NASA NAG 5-3057. The calculations reported here were performed at the Pittsburgh Supercomputing Center.

REFERENCES

- Aarseth, S. J. 1972, in *Gravitational N-body Problem*, IAU Colloquium No. 10, ed. M. Lecar (Dordrecht: Reidel), 373
- Binney, J. & Tremaine, S. 1987, *Galactic Dynamics* (Princeton, NJ: Princeton Univ. Press)
- Brandt, A. 1977, *Math. Comp.*, 31, 333
- Briel, U. G. et al. 1991, *A&A*, 246, L10
- Bryan, G. L., Cen, R. Y., Norman, M. L., Ostriker, J. P., & Stone, J. M. 1994, *ApJ*, 428, 405
- Burns, J. O., Roettiger, K., Ledlow, M., & Klypin, A. 1994, *ApJ*, 427, L87
- Cavaliere, A. & Fusco-Femiano, R. 1976, *A&A*, 49, 137
- Chandrasekhar, S. 1961, *Hydrodynamic and Hydro-magnetic Stability* (Oxford: Clarendon)
- Colella, P. & Woodward, P. 1984, *J. Comp. Phys.*, 54, 174
- David, L. P., Jones, C., & Forman, W. 1995, *ApJ*, 445, 578
- de Vaucouleurs, G. 1948, *Ann. d'Ap.*, 11, 247
- Dubinski, J. & Carlberg, R. G. 1991, *ApJ*, 378, 496
- Elbaz, D., Arnaud, M., & Böhringer, H. 1995, *A&A*, 293, 337
- Evrard, A. E. 1990, *ApJ*, 363, 349
- Evrard, A. E., Metzler, C. A., & Navarro, J. F. 1996, *ApJ*, 469, 494
- Forman, W. & Jones, C. 1994, in *Cosmological Aspects of X-Ray Clusters of Galaxies*, ed. W. C. Seitzer (Dordrecht: Kluwer), 39
- Hackbusch, W. 1985, *Multi-Grid Methods and Applications* (Berlin: Springer-Verlag)
- Henriksen, M. J. & Markevitch, M. L. 1996, *ApJ*, 466, L79
- Hernquist, L. 1987, *ApJS*, 64, 715
- Hernquist, L. 1990, *ApJ*, 356, 359
- Hernquist, L. 1992, *ApJ*, 400, 460
- Hernquist, L. 1993, *ApJ*, 409, 548
- Hoffman, Y. & Shaham, J. 1985, *ApJ*, 297, 16
- James, R. A. 1977, *J. Comp. Phys.*, 25, 71
- Kang, H., Ostriker, J. P., Cen, R., Ryu, D., Hernquist, L., Evrard, A. E., Bryan, G. L., & Norman, M. L. 1994, *ApJ*, 430, 83
- Katz, N. & White, S. D. M. 1993, *ApJ*, 412, 455
- Landau, L. D. & Lifschitz, E. M. 1987, *Fluid Mechanics*, 2d ed. (Oxford: Pergamon)
- Markevitch, M. 1996, *ApJ*, 465, L1
- Navarro, J. F., Frenk, C. S., & White, S. D. M. 1996, *ApJ*, 462, 563
- Pearce, F. R., Thomas, P. A., & Couchman, H. M. P. 1994, *MNRAS*, 268, 953
- Peebles, P. J. E. 1993, *Principles of Physical Cosmology* (Princeton, NJ: Princeton Univ. Press)
- Press, W. H. & Schechter, P. 1974, *ApJ*, 187, 425
- Richstone, D., Loeb, A., & Turner, E. L. 1992, *ApJ*, 393, 477
- Roettiger, K., Burns, J., & Loken, C. 1993, *ApJ*, 407, L53
- Roettiger, K., Stone, J., & Mushotzky, R. 1997, preprint astro-ph/9708043
- Rybicki, G. B. & Lightman, A. P. 1979, *Radiative Processes in Astrophysics* (New York: Wiley)
- Schindler, S. & Müller, E. 1993, *A&A*, 272, 137
- Sedov, L. I. 1959, *Similarity and Dimensional Methods in Mechanics* (New York: Academic)
- Strang, G. 1968, *SIAM J. Numer. Anal.*, 5, 506
- White, D. A. & Fabian, A. C. 1995, *MNRAS*, 273, 72
- White, S. D. M., Briel, U. G., & Henry, J. P. 1993, *MNRAS*, 261, L8